The dynamic organic p-n junction

Piotr Matyba, Klara Maturova, Martijn Kemerink, Nathaniel D Robinson and Ludvig Edman

Original Publication:

Piotr Matyba, Klara Maturova, Martijn Kemerink, Nathaniel D Robinson and Ludvig Edman, The dynamic organic p-n junction, 2009, NATURE MATERIALS, (8), 8, 672-676.
http://dx.doi.org/10.1038/NMAT2478

The Dynamic Organic p-n Junction

Piotr Matyba[1], Klara Maturova[2], Martijn Kemerink[2], Nathaniel D. Robinson[3] and Ludvig Edman[1,*]

[1] The Organic Photonics and Electronics Group, Dept. of Physics, Umeå University, SE-901 87 Umeå, Sweden

[2] Dept. of Applied Physics, Eindhoven University of Technology, P.O. Box 513, 5600 MB, Eindhoven, The Netherlands

[3] The Transport and Separations Group, Dept. of Phys. Chem. and Bio., Linköping University, SE-58183 Linköping, Sweden

* Corresponding author, e-mail address: ludvig.edman@physics.umu.se

Abstract

Static p-n junctions in inorganic semiconductors are exploited in a wide range of today's electronic appliances. Here, we demonstrate the *in-situ* formation of a *dynamic* p-n junction structure within an organic semiconductor through electrochemistry. Specifically, we utilize scanning Kelvin probe microscopy and optical probing on planar light-emitting electrochemical cells (LECs) with a mixture of a conjugated polymer and an electrolyte connecting two electrodes separated by 120 μm. We find that a significant portion of the potential drop between the electrodes coincides with the location of a thin and distinct light-emission zone positioned >30 μm away from the negative electrode. These results are relevant in the context of a long-standing scientific debate, since they prove that electrochemical doping can take place in LECs. Moreover, a study on the doping formation and dissipation kinetics provides interesting detail regarding the electronic structure and stability of the dynamic organic p-n junction, which may be useful in future dynamic p-n junction-based devices.

Organic semiconductors are heralded for their simple processing and extraordinary chemical customizability, and emerging low-cost and flexible devices based on these materials are expected to revolutionize the role electronics play in our everyday lives.[1, 2] Some devices are already commercially available — a notable example being the organic light-emitting diode (OLED) in television and cell phone displays — but it is clear that further opportunities exist beyond the current state-of-the-art. For instance, the soft nature of organic semiconductors can allow *in-situ* electrochemical tuning of important material properties.[3-13] One device that exploits this opportunity in an attractive manner is the light-emitting electrochemical cell (LEC).[14-22] The nominal difference between an LEC and an OLED is that the former contains mobile ions in the active material.[23-30] These ions rearrange during operation, which in turn allows for a range of attractive device properties, including low-voltage operation with thick active layers and stable electrode materials.[31-36]

However, the further development of LECs is currently hampered by an inadequate understanding of the device operation. In fact, an active debate regarding the fundamental nature of LEC operation has continued for more than a decade, and two distinct models are competing for acceptance: the electrochemical doping model[18, 32, 37-40] and the electrodynamic model[36, 41-44]. In order to distinguish them, it is appropriate to establish the electrostatic potential profile in a device during steady-state operation, as the models predict distinctly differing profiles. The electrodynamic model predicts that the entire applied potential will drop over thin electric double layers (EDLs) at the electrode/active material interfaces, while the electrochemical doping model predicts that a significant fraction of the applied potential will drop over a light-emitting p-n junction. Thus, in order to discriminate between the two models, it is essential to record the potential profile within an LEC device where the light emission zone is positioned away from the electrode/active material interfaces.

Two attempts to measure the electrostatic potential within an LEC device during operation have been published. Slinker *et al.*[43] employed electric force microscopy on a planar LEC, with an ionic organometallic semiconductor as the active material. Although their measurements have been questioned, primarily because light-emission and the potential profile were observed under rather differing experimental conditions,[37] they demonstrated that such direct potential measurements could be performed in planar devices. In a more recent report, Pingree *et al.*[45] used scanning Kelvin probe microscopy (SKPM) on planar LECs containing a mixture of a conjugated polymer and a solid-state electrolyte as the active material. They did not report any light emission data, and the presented potential profiles were unfortunately inconclusive in that the potential drop was positioned at the negative electrode interface, and as such in effect consistent with both proposed models of operation.

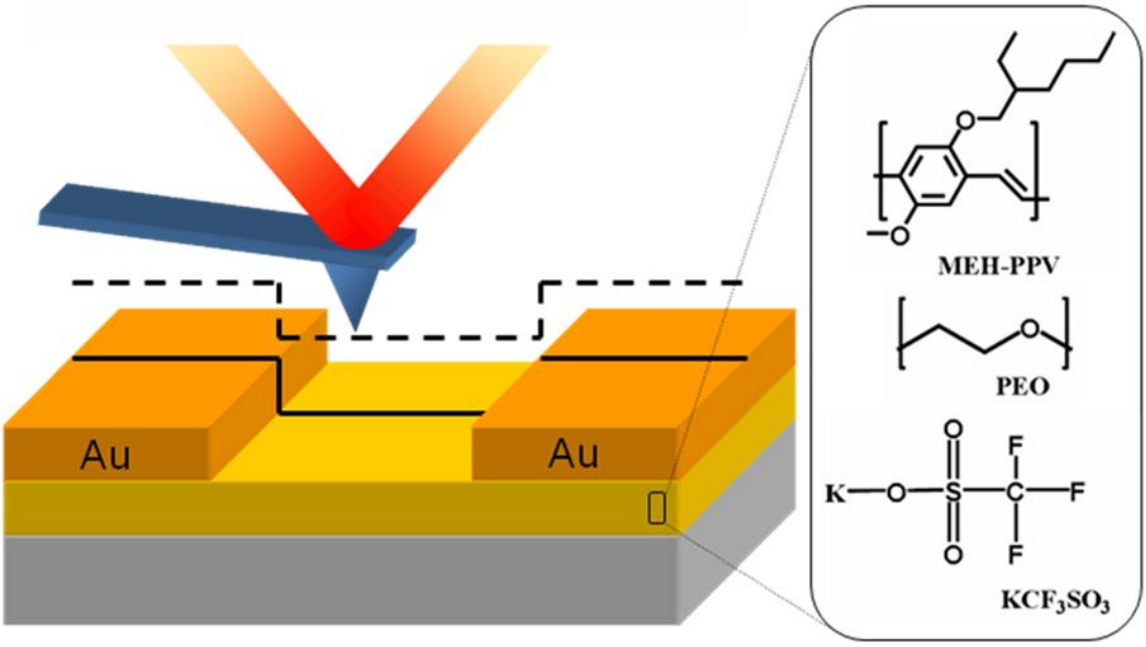

Figure 1. *Schematic illustrating the probing of a planar LEC device with SKPM. The solid line marks the topographic scan and the dashed line indicates the SKPM scan in lift mode. The active material components are included in the inset to the right.*

In this article, we utilize the SKPM technique in parallel with light-emission detection on planar LEC devices, comprised of an active material mixture of poly[2-methoxy-5-(2-ethylhexyloxy)-1,4-phenylenevinylene] (MEH-PPV) + poly(ethylene oxide) (PEO) + KCF_3SO_3 positioned between two Au electrodes, where the latter define an inter-electrode gap of 120 μm. Figure 1 shows a schematic illustrating the SKPM probing of a planar device on the left and the active material constituents in the subset on the right. Because we employed a perpendicular tip/electrode geometry, which may lead to artifacts when interpreting SKPM data, we also performed a deconvolution (see Supplementary material) that demonstrated that the recorded potential profiles are at least qualitatively correct. Importantly, we performed SKPM measurements and light emission probing under similar conditions on separate sets of LEC devices (see methods section for details), in which the light emission zone is positioned far away from the electrode/active material interfaces.[35, 39] As motivated above, the latter is critical in order to distinguish between the two models. It is made possible in these experiments by the use of an appropriate organic semiconductor-electrolyte active material driven with a relatively high voltage, so that undesired electrochemical side-reactions at the electrode/active material interfaces are effectively suppressed.[46, 47]

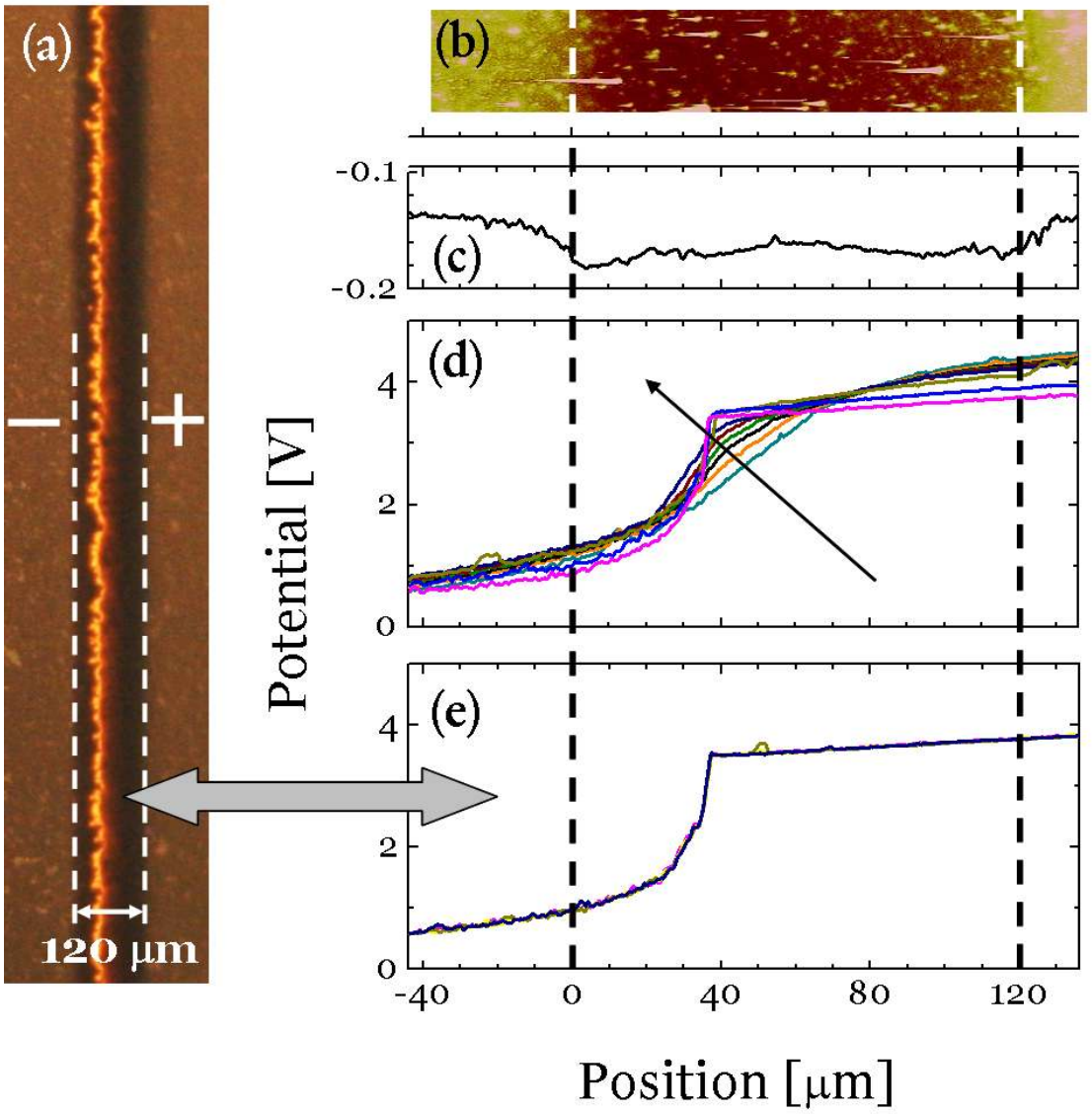

Figure 2. *(a) Micrograph showing the light emission from a planar LEC device during steady-state operation at V = 5 V; the positive and negative electrodes are indicated by the + and – sign, respectively. (b) 2D topographic image of an identical planar LEC device. (c) Electrostatic potential profile recorded on a pristine device under open-circuit conditions. (d) Temporal evolution of the potential profile during the initial operation at V = 5 V; the arrow indicates increasing time. The time delay between successive potential profiles was ~20 s. (e) The subsequent steady-state potential profile recorded at V = 5 V.*

Figure 2a is an optical micrograph of an LEC device taken at t = 300 s after an external voltage of V = 5 V was applied. A distinct light-emission zone is apparent in the bulk of the active material at a distance d ~ 35 μm away from the negative Au electrode interface. Figures 2b and 2c present the 2D topography image and the potential profile at open circuit, respectively, recorded on an identical device.

The structure in the potential profile is due to a minor charge transfer between the Au electrodes and the MEH-PPV polymer. The two interfaces between the electrodes and the active material are clearly distinguishable at d = 0 μm and d = 120 μm and indicated by the vertical dashed lines. AFM data demonstrating the sharpness of this interface are included in the supplementary material.

Figures 2d and 2e present the temporal evolution of the potential profile up to t = 180 s (with increasing time indicated by the arrow) and between t = 180 s and t = 600 s, respectively, for the same device during operation at V = 5 V. The potential profile changes from dropping essentially linearly between the two electrodes at t ~ 10 s (first line scan in Fig. 2d) to reach steady-state (potential profile changes very little over several minutes) at $t \geq 180$ s (last line scan in Fig. 2d and Fig. 2e), where the steepest potential drop is localized over a limited spatial region centered at d ~ 35 μm. It is notable that the spatial position of this potential drop coincides very well with the location of the light emission zone in panel a. The corresponding current measurement is included as Fig. S2 in the supplementary material.

At this stage, it is relevant to consider the key steps within the *electrochemical doping model*. (i) Following the application of an external voltage, thin EDLs form at the electrode/active material interfaces; (ii) if the applied voltage is sufficiently large ($V \geq E_g/e$, where E_g is the band gap of the organic semiconductor and e is the elementary charge), holes and electrons are injected into the organic semiconductor via the EDLs at the positive and negative electrodes, respectively; (iii) the injected electronic charge carriers attract electrostatically compensating ions, which establish doped regions with high conductivity at the two electrode interfaces; (iv) a p-type doping front (comprising holes and compensating anions) and an n-type doping front (comprising electrons and cations) grow towards each other and, after a turn-on time, make contact, forming a p-n junction; (v) subsequently injected holes and electrons migrate through the doped regions and recombine within, or in close proximity of, the undoped p-n junction, causing the emission of light.[32, 38]

The *electrodynamic model* includes the first two steps above, but, notably, does not include any electrochemical doping, and hence no conductivity increase or p-n junction formation. Instead, it claims that the electronic charge carriers are driven by diffusion in the undoped bulk of the active material, and importantly that the potential drops at steady-state are localized at the electrode interfaces.[41, 42]

However, our observation of a significant localized potential drop positioned in the bulk of the active material, far away from the electrode interfaces, at steady state (see Fig. 2e) directly contradicts the electrodynamic model. In contrast, the observation of a localized potential drop in the bulk that spatially coincides with a distinct light-emitting zone is consistent with the existence of a forward-biased p-n junction (as schematically illustrated in Fig. 4b). Thus, the presented data provide strong evidence that LEC devices can operate in a manner consistent with the electrochemical doping model.

We note that we do not detect the formation of EDLs at the metal electrode interfaces during the initial operation of these devices (as predicted by both models). We propose, based on XPS data and the temporal evolution of recorded AFM phase data (see Figs. S3 and S4 and the corresponding discussion in the supplementary material) as well as the absence of an interfacial potential drop between the negative Au electrode and the n-type doped material at steady-state, that this is due to the existence of a thin layer of ion-containing material on top of the electrodes that screens some of the potential.

We also wish to call attention to a number of interesting features of the probed dynamic organic p-n junction structure. First, both the light-emission data and the potential profiles indicate that the effective p-n junction is broad, with a width on the order of 10 μm. Second, the slope in the potential profile at steady-state is notably steeper on the n-type side of the junction than on the p-type side (see Fig. 2e). We believe that the latter is an indication of the conductivity difference between the n-doped and the p-doped MEH-PPV. The n-doped material appears to be less conducting, so that a larger potential gradient is necessary on the n-type side in order to provide a constant current density across the device at steady state.

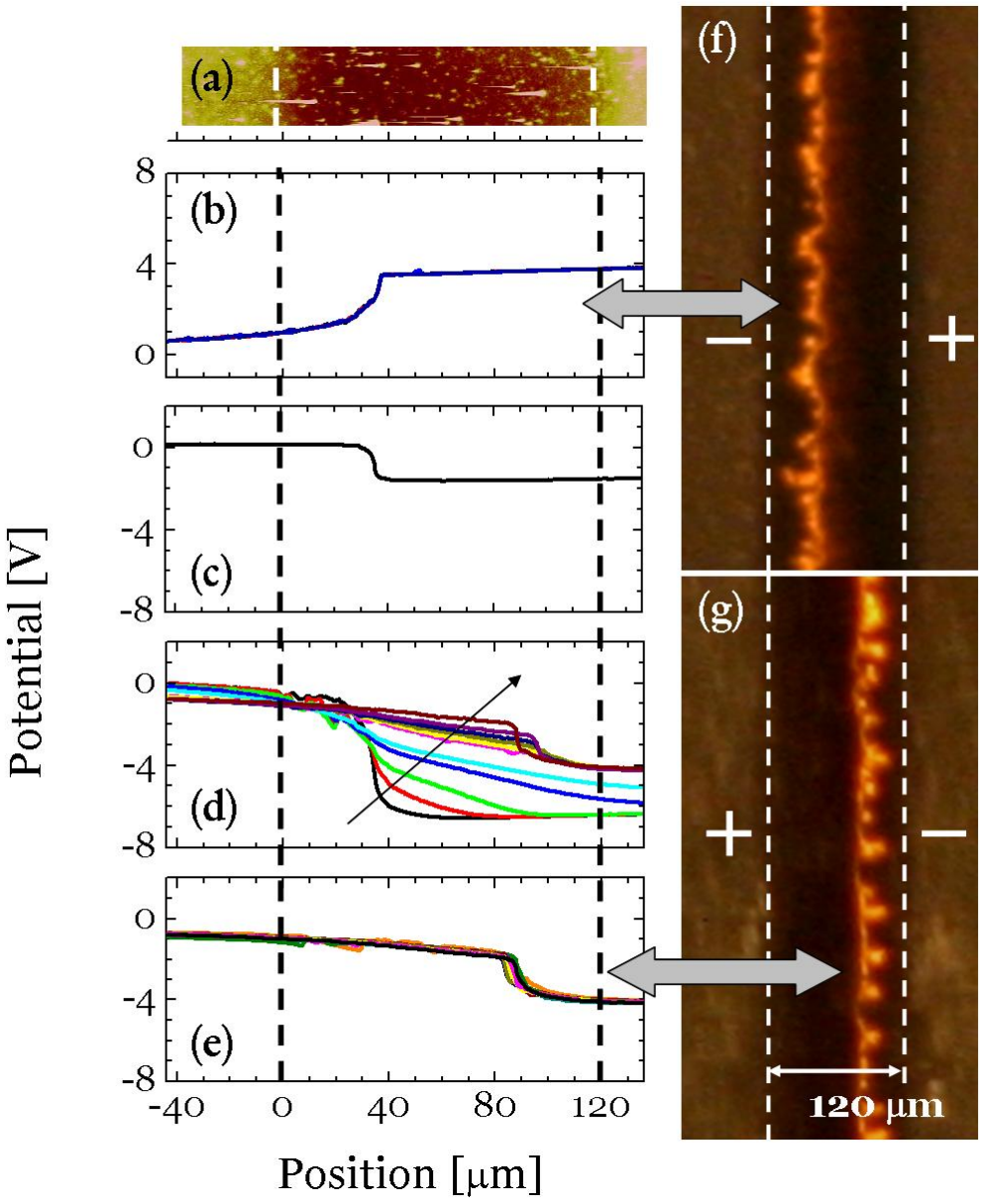

Figure 3. *(a) 2D topography image of a planar LEC device. (b) Electrostatic potential profile during steady-state operation at V = +5 V. (c) Transient potential profile measured with the device disconnected (open circuit), directly after long-term operation at V = +5 V. (d) Temporal evolution of the potential profile after a subsequent switch to V = -5 V; the arrow indicates increasing time. (e) Steady-state potential profile at V = -5 V. (f) Micrograph showing the light emission during steady-state operation at V = +5 V. (g) Subsequent micrograph showing the light emission from the same device during steady-state operation at V = -5 V.*

In order to obtain more detailed information on the structure and stability of the dynamic p-n junction and the kinetics and reversibility of the doping process, we

have investigated the effects of shifting the voltage applied to a device operating at steady-state. Figure 3a shows a 2D topography image that, together with potential images at open circuit (not shown) and micrographs, identifies the positions of the electrode interfaces as indicated by the vertical dashed lines. Figures 3b and 3f present the potential profile and a micrograph recorded at steady state at a "forward bias" of V = +5 V. A direct correlation between a significant potential drop in the bulk of the active material and the location of the emission zone is once again observed. The device was thereafter left disconnected at open circuit (impedance > 100 MOhm) for a brief period of time (~30 s), and the first recorded potential profile after disconnection is included as Figure 3c. Finally, a "reverse bias" of V = -5 V was applied. Figure 3d presents the temporal evolution of the potential between t = 0 s and t = 1800 s following the application of the reverse bias (the arrow indicates increasing time). Figures 3e and 3g present the subsequent steady-state potential profile at $t \geq$ 1800 s and a micrograph recorded at t = 1920 s, respectively.

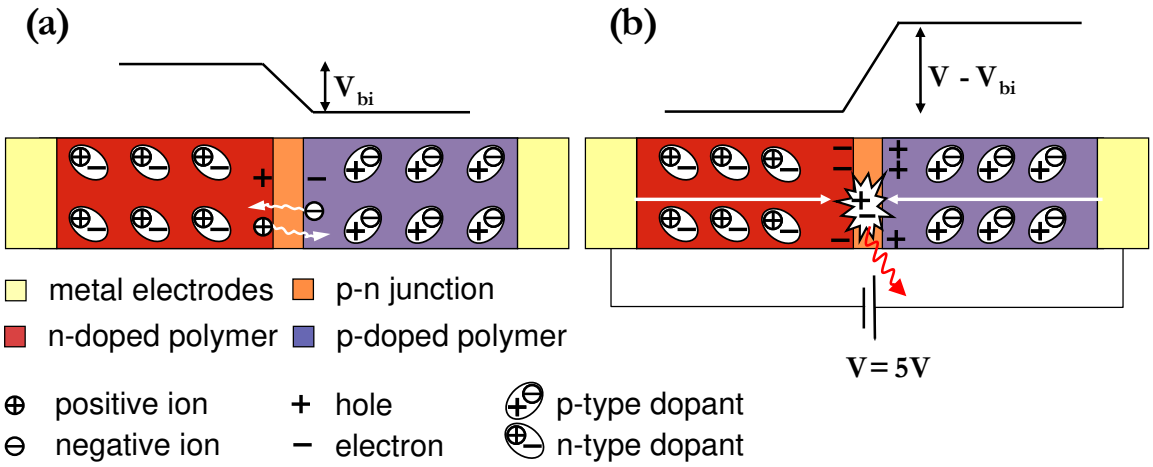

Figure 4. *Schematics illustrating the electrostatic profile (top part) and the electronic and ionic charge distribution (bottom part) within a p-n junction structure established at V = +5 V. The net charge motion is indicated by the white arrows. (a) shows the transient charge distribution and initial ionic motion directly after a shift to open-circuit condition, where V_{bi} indicates the built-in potential over the junction. (b) shows the steady-state charge distribution, electronic motion and radiative recombination at V = +5 V.*

To facilitate a discussion of the recorded data in Fig. 3, two schematics are presented in Figure 4. First, we note that the steady-state potential profile and the position of the light-emission zone in the inter-electrode gap at V = -5 V (recorded at the end of the measurement) are essentially mirror images of those at V = +5 V. This implies that all of the relevant processes are highly reversible under the conditions and the time scale of this study, and that the effects of chemical and electrochemical side reactions can be excluded from the coming discussion.

We note with interest that Fig. 3c reveals a potential drop of ~ 1.5 V at the location of the p-n junction, immediately after the long-term, steady-state operation voltage of V = +5 V is disconnected (the circuit is opened). This

observation is consistent with the existence of a built-in potential of $V_{bi} \sim 1.5$ V (which is slightly lower than the band-gap potential, $V_{BG} = E_g/e$, of the employed semiconductor, MEH-PPV[48]) over the p-n junction, with a polarity opposite that of the applied voltage that built the p-n junction. We propose, in analogy with the well-established physics of p-n junctions in inorganic crystalline semiconductors, that V_{bi} can be attributed to an equilibration of electronic charge carriers over the junction region. More specifically, one can envision the establishment of a diffusion-drift balance for the electrons over a p-n junction at open circuit, resulting in a uniform electrochemical potential for the electrons (or Fermi level) throughout the device, as follows: "Fast" electrons diffuse from the n-type side to the p-type side leaving "slow" cations behind; this process establishes a potential drop V_{bi} over the junction, which causes an equal and opposite drift of electrons from the p-type side to the n-type side. (An equivalent set of events involving "fast" holes and "slow" anions will simultaneously take place.)

Figure 4a presents the electrostatic potential (top part) and a schematic of the doping structure and the charge separation over a p-n junction at open circuit, which rationalizes the recorded potential profile shown in Fig. 3c. Fig. 4a also indicates the onset of net ionic motion over the junction, which motivates the transient character of the potential profile. This relaxation process, which is a manifestation of the non-equilibrated electrochemical potential for the ions over the junction, is further discussed below.

The existence of V_{bi} over the junction region also explains why the probed potential V_{tot} over the p-n junction under steady-state conditions is smaller than the applied potential V (see, *e.g.,* Fig. 3b). The potential probed with SKPM corresponds to the total electrostatic potential within the device, which here is a combination of the externally applied potential and the built-in potential, where the latter at steady state has a sign opposing the former; *i.e.,* $V_{tot} = V - V_{bi}$ (see top part in Fig. 4b). The net charge separation over the junction region, as well as the charge transport and radiative recombination, in a planar LEC device at steady-state is depicted in Figure 4b. The existence of V_{bi} also explains why the probed potential is larger than the applied voltage following a fast switch in the polarity of the applied voltage (from +5 V to − 5 V in Fig. 3d). Here, the applied voltage and the built-in potential are temporarily oriented in the same direction, and the total probed potential is accordingly $V_{tot} = V + V_{bi} > V$.

The p-n junctions discussed here are distinctly different from conventional p-n junctions in, *e.g.,* Si, in that the compensating, and dopant-stabilizing, counter-ions are mobile. Thus, these novel doping structures are appropriately termed *dynamic* p-n junctions, whereas conventional p-n junctions are static structures. The mobility of the ions allows the dynamic p-n junction to be formed *in-situ*, but also means that the doping and junction will dissipate and/or reform in response to a shift in the external applied voltage, as demonstrated in Fig. 3. The latter redistribution processes involve a complicated interplay of electronic and ionic motion, as exemplified in the complex evolution of the potential profiles in Fig. 3d following a shift in the applied voltage.

We further note that a dynamic p-n junction can only be stable above a critical applied voltage exceeding the built-in potential, $V > V_{bi}$, since the ionic concentration gradients and the accompanying doping profiles will dissipate at a lower voltage. A simple example involving the stability of the cationic concentration gradient can illustrate this point (but the same argument holds for the anionic gradient as well): The cations on the n-type side of the p-n junction exhibit a net diffusive motion towards the p-type side (due to the cationic concentration gradient over the junction), and this diffusive motion can only be compensated by a drift motion of cations in the opposite direction if the total electrostatic potential over the junction (the sum of V and V_{bi}) drives the cations in the direction opposing the concentration gradient. Thus, since V_{bi} opposes V under steady-state conditions, it follows directly that $V > V_{bi}$ is the prerequisite for a stable dynamic p-n junction structure. One scenario under which the ionic concentration gradients and the junction structure are unstable (*i.e.,* $V < V_{bi}$) is illustrated in Fig. 4a, while Fig. 4b shows a situation ($V = 5$ V $> V_{bi}$) at which the p-n junction structure is stable.

Finally, it is appropriate to mention that the primary differences between the experiments presented here and those of our predecessors is the chemical system employed and the conditions under which the measurements were made. We have previously demonstrated that the use of small Li^+ cations and/or the application of low voltages in conjugated polymer-based LECs can negatively impact the placement of the p-n junction, leaving it very near the negative metal electrode.[35, 46] This is plausibly the reason why Pingree *et al.*[45] observed a different potential profile than we do. The Ruthenium-based ionic transition metal complex used by Slinker *et al.*[43] in their light-emitting device differs chemically from the MEH-PPV conjugated polymer presented here. It is not clear, for example, that this type of transition metal complex can be doped into a highly conductive state, which would result in an operational mechanism unlike that observed in conjugated-polymer LECs.

Conclusions

We have utilized a combination of SKPM and light emission probing to establish that a p-n junction can form *in-situ* in the bulk of the active material of an LEC device during operation. This observation provides evidence that the so-called electrochemical doping model can describe the operation of LECs, which is relevant in the context of an ongoing debate in the scientific literature. Moreover, the availability of a dynamic organic p-n junction opens the possibility for interesting fundamental physics. For example, we demonstrate the existence of a built-in potential over the junction, which must be compensated by an external voltage in order to stabilize the junction structure. Finally, we note that the tantalizing subject of dynamic organic p-n junctions is largely unexplored, and that further studies in this field could open a wide range of novel and useful applications.

Methods

The conjugated polymer poly[2-methoxy-5-(2-ethylhexyloxy)-1,4-phenylenevinylene] (MEH-PPV, M_w = 150.000 g/mol, Aldrich) and poly(ethylene oxide) (PEO, M_w = 5x10^6 g/mol, Aldrich) were used as received. The salt KCF_3SO_3 (98%, Alfa Aesar) was dried at a temperature (T) of 473 K under N_2 atmosphere before use. Master solutions were prepared in a concentration of 10 mg/ml by dissolving MEH-PPV in chloroform (>99%, anhydrous, Aldrich), and by dissolving PEO and KCF_3SO_3 separately in cyclohexanone (99%, Merck). A blend solution was prepared by mixing the master solutions together in a mass ratio of MEH-PPV:PEO:KCF_3SO_3 = 1:1.35:0.25, followed by stirring on a magnetic hot plate at T = 323 K for 12 h. The glass substrates (1×1 cm^2) were cleaned by subsequent ultrasonic treatment in detergent, acetone and isopropanol.

The glass substrates were spin coated with the blend solution (at 800 rpm for 60 s, followed by 1000 rpm for 10 s), and thereafter dried on a hot plate at T = 320 K for 12 h. The resulting active material film had a thickness of ~300 nm, as established with AFM. Au electrodes were deposited on top of the active material by thermal evaporation of Au under high vacuum (p ~1×10^{-6} mBar); the inter-electrode gap of 120 μm was established with an Al shadow mask positioned in close proximity to the active material. The sharpness of the Au electrode interfaces has been confirmed by AFM, as described in the supplementary material. All fabrication steps, excluding the cleaning of substrates, were done in two interconnected glove boxes filled with N_2 ([O2] < 1 ppm and [H2O] < 1 ppm).

The optical probing of the light emission zone was performed at room temperature in two different setups: (i) in an optical-access cryostat under high vacuum (p <10^{-5} mBar), using a SLR camera (Canon EOS20) equipped with a macro lens (focal length: 65 mm) and a teleconverter (2x), (ii) in a glove box under the same conditions as the SKPM measurements (see below), using an optical microscope equipped with a video camera (Hengtech). We find that the device data, notably the position of the light emission zone in the interelectrode gap, is effectively the same in both set-ups, and we chose to present the data acquired in the cryostat due to image quality. In parallel with the optical probing, the current was measured with a computer controlled source-measure unit (Keithley 2400).

All SKPM images were recorded in a glove box under N2 atmosphere ([O2] < 1 ppm and [H2O] < 1 ppm) with a commercial AFM system (Veeco Instruments MultiMode AFM with Nanoscope IV controller) operating in Lift Mode; *i.e.,* each line is scanned twice, first to measure topography in Tapping Mode (oscillation amplitude setpoint over free amplitude $A/A_0 \approx 1.4/1.8$) and second to measure the electrostatic potential (using amplitude modulation at the first resonance of the cantilever, with V_{ac} = 8 V and V_{dc} applied to the cantilever) at a predefined lift height. We used zero lift height, which results in a typical tip-sample gap of about 15 nm. We employed sharp silicon tips with a Pt coating (Olympus OMCL-AC240TM-B2, apex radius < 15 nm, k ~ 2 N/m, cone angle < 25°, resonant

frequency ~ 70 kHz). The scan rate was 0.2 Hz, so each line takes 2×5 seconds to scan. Tip coarse positioning and in-situ electroluminescence detection were performed via a CCD camera attached to a long working-distance microscope inside the glove box. The parallel electrical characterization was performed with a Keithley 4200 unit connected to the SKPM via an electrical port in the glove box. All measurements were performed at room temperature.

References

1. Forrest, S. R. The path to ubiquitous and low-cost organic electronic appliances on plastic. Nature 428, 911-918 (2004).

2. Malliaras, G. & Friend, R. An organic electronics primer. Phys Today 58, 53-58 (2005).

3. Moller, S., Perlov, C., Jackson, W., Taussig, C. & Forrest, S. R. A polymer/semiconductor write-once read-many-times memory. Nature 426, 166-169 (2003).

4. Leger, J. M. Organic electronics: The ions have it. Adv Mater 20, 837-841 (2008).

5. Yazaki, S., Funahashi, M. & Kato, T. An electrochromic nanostructured liquid crystal consisting of pi-conjugated and ionic moieties. J Am Chem Soc 130, 13206-13207 (2008).

6. Gao, L., Johnston, D. & Lonergan, M. C. Synthesis and self-limited electrochemical doping of polyacetylene ionomers. Macromolecules 41, 4071-4080 (2008).

7. Wei, D. & Amaratunga, G. Photoelectrochemical cell and its applications in optoelectronics. Int J Electrochem Sci 2, 897-912 (2007).

8. Leger, J. M., Patel, D. G., Rodovsky, D. B. & Bartholomew, G. P. Polymer photovoltaic devices employing a chemically fixed p-i-n junction. Adv Funct Mater 18, 1212-1219 (2008).

9. Edman, L., Swensen, J., Moses, D. & Heeger, A. J. Toward improved and tunable polymer field-effect transistors. Appl Phys Lett 84, 3744-3746 (2004).

10. Lin, F. D. & Lonergan, M. C. Gate electrode processes in an electrolyte-gated transistor: Non-faradaically versus faradaically coupled conductivity modulation of a polyacetylene ionomer. Appl Phys Lett 88, 133507 (2006).

11. Lu, W. et al. Use of ionic liquids for pi-conjugated polymer electrochemical devices. Science 297, 983-987 (2002).

12. Beaujuge, P. M., Ellinger, S. & Reynolds, J. R. The donor-acceptor approach allows a black-to-transmissive switching polymeric electrochrome. Nat Mater 7, 795-799 (2008).

13. Kaihovirta, N. J., Tobjork, D., Makela, T. & Osterbacka, R. in European Congress and Exhibition on Advanced Materials and Processes (Euromat 2007) 640-643 (Wiley-V C H Verlag Gmbh, Nurnberg, GERMANY, 2007).

14. Shin, J. H., Xiao, S., Fransson, A. & Edman, L. Polymer light-emitting electrochemical cells: Frozen-junction operation of an "ionic liquid" device. Appl Phys Lett 87, 043506 (2005).

15. Latini, G. et al. Cyclodextrin-threaded conjugated polyrotaxanes for organic electronics: The influence of the counter cations. Adv Funct Mater 18, 2419-2427 (2008).

16. Hohertz, D. & Gao, J. How electrode work function affects doping and electroluminescence of polymer light-emitting electrochemical cells. Adv Mater 20, 3298-3302 (2008).

17. Alem, S. & Gao, J. The effect of annealing/quenching on the performance of polymer light-emitting electrochemical cells. Org Electron 9, 347-354 (2008).

18. Pei, Q. B., Yu, G., Zhang, C., Yang, Y. & Heeger, A. J. Polymer Light-Emitting Electrochemical-Cells. Science 269, 1086-1088 (1995).

19. Gao, J. & Dane, J. Planar polymer light-emitting electrochemical cells with extremely large interelectrode spacing. Appl Phys Lett 83, 3027-3029 (2003).

20. Gao, J. & Dane, J. Visualization of electrochemical doping and light-emitting junction formation in conjugated polymer films. Appl Phys Lett 84, 2778-2780 (2004).

21. Graber, S. et al. A Supramolecularly-Caged Ionic Iridium(III) Complex Yielding Bright and Very Stable Solid-State Light-Emitting Electrochemical Cells. J Am Chem Soc 130, 14944-14945 (2008).

22. Shao, Y., Bazan, G. C. & Heeger, A. J. Long-lifetime polymer light-emitting electrochemical cells. Adv Mater 19, 365-370 (2007).

23. Jin, Y., Bazan, G. C., Heeger, A. J., Kim, J. Y. & Lee, K. Improved electron injection in polymer light-emitting diodes using anionic conjugated polyelectrolyte. Appl Phys Lett 93, 123304 (2008).

24. Yu, M. X., Kang, J. H. & Cheng, C. H. Synthesis of diarylamino-benzo[de]anthracen-7-ones and their light emitting property. Chin J Org Chem 28, 1393-1397 (2008).

25. Jin, Y. et al. Novel green-light-emitting polymers based on cyclopenta[def]phenanthrene. Macromolecules 41, 5548-5554 (2008).

26. Oh, S. H., Vak, D., Na, S. I., Lee, T. W. & Kim, D. Y. Water-soluble polyfluorenes as an electron injecting layer in PLEDs for extremely high quantum efficiency. Adv Mater 20, 1624-1629 (2008).

27. Sun, J. et al. pi-Conjugated poly(anthracene-alt-fluorene)s with X-shaped repeating units: New blue-light emitting polymers. Polymer 49, 2282-2287 (2008).

28. Ortony, J. H. et al. Thermophysical properties of conjugated polyelectrolytes. Adv Mater 20, 298-302 (2008).

29. Shao, Y., Bazan, G. C. & Heeger, A. J. LED to LEC transition behavior in polymer light-emitting devices. Adv Mater 20, 1191-1193 (2008).

30. Hoven, C. et al. Ion motion in conjugated polyelectrolyte electron transporting layers. J Am Chem Soc 129, 10976-10977 (2007).

31. Sun, Q. J., Li, Y. F. & Pei, Q. B. Polymer light-emitting electrochemical cells for high-efficiency low-voltage electroluminescent devices. J Disp Technol 3, 211-224 (2007).

32. Edman, L. Bringing light to solid-state electrolytes: The polymer light-emitting electrochemical cell. Electrochimica Acta 50, 3878-3885 (2005).

33. Shin, J. H. et al. Light emission at 5 V from a polymer device with a millimeter-sized interelectrode gap. Appl Phys Lett 89, 013509 (2006).

34. Shin, J. H. & Edman, L. Light-emitting electrochemical cells with millimeter-sized interelectrode gap: Low-voltage operation at room temperature. J Am Chem Soc 128, 15568-15569 (2006).

35. Shin, J. H., Robinson, N. D., Xiao, S. & Edman, L. Polymer light-emitting electrochemical cells: Doping concentration, emission-zone position, and turn-on time. Adv Funct Mater 17, 1807-1813 (2007).

36. Slinker, J. D. et al. Electroluminescent devices from ionic transition metal complexes. J Mater Chem 17, 2976-2988 (2007).

37. Pei, Q. & Heeger, A. J. Operating mechanism of light-emitting electrochemical cells. Nat Mater 7, 167-167 (2008).

38. Pei, Q. B., Yang, Y., Yu, G., Zhang, C. & Heeger, A. J. Polymer light-emitting electrochemical cells: In situ formation of a light-emitting p-n junction. J Am Chem Soc 118, 3922-3929 (1996).

39. Robinson, N. D., Shin, J. H., Berggren, M. & Edman, L. Doping front propagation in light-emitting electrochemical cells. Phys Rev B 74, 155210 (2006).

40. Dick, D. J., Heeger, A. J., Yang, Y. & Pei, Q. B. Imaging the structure of the p-n junction in polymer light-emitting electrochemical cells. Adv Mater 8, 985-987 (1996).

41. deMello, J. C. Interfacial feedback dynamics in polymer light-emitting electrochemical cells. Phys Rev B 66, 235210 (2002).

42. deMello, J. C., Tessler, N., Graham, S. C. & Friend, R. H. Ionic space-charge effects in polymer light-emitting diodes. Phys Rev B 57, 12951-12963 (1998).

43. Slinker, J. D. et al. Direct measurement of the electric-field distribution in a light-emitting electrochemical cell. Nat Mater 6, 894-899 (2007).

44. Malliaras, G. G. et al. Operating mechanism of light-emitting electrochemical cells - Authors' response. Nat Mater 7, 168-168 (2008).

45. Pingree, L. S. C., Rodovsky, D. B., Coffey, D. C., Bartholomew, G. P. & Ginger, D. S. Scanning kelvin probe imaging of the potential profiles in fixed and dynamic planar LECs. J Am Chem Soc 129, 15903-15910 (2007).

46. Fang, J., Matyba, P., Robinson, N. D. & Edman, L. Identifying and alleviating electrochemical side-reactions in light-emitting electrochemical cells. J Am Chem Soc 130, 4562-4568 (2008).

47. Matyba, P., Andersson, M. R. & Edman, L. On the desired properties of a conjugated polymer-electrolyte blend in a light-emitting electrochemical cell. Org Electron 9, 699-710 (2008).

48. Holt, A. L., Leger, J. M. & Carter, S. A. Electrochemical and optical characterization of p- and n-doped poly[2-methoxy-5-(2-ethylhexyloxy)-1,4-phenylenevinylene]. J Chem Phys 123, 044704 (2005).

Supplementary information accompanies this paper on www.nature.com/naturematerials

Acknowledgements

LE and PM acknowledge the Swedish Research Council (VR) and Wenner-Gren stiftelserna for scientific funding. LE is a “Royal Swedish Academy of Sciences Research Fellow” supported by a grant from the Knut and Alice Wallenberg Foundation. NDR acknowledges VR and Norrköpings Kommun for funding of part of this work. The work of KM is made possible by a NanoNed grant (NanoNed is the Dutch nanotechnology initiative by the Ministry of Economic Affairs). The authors acknowledge Dr. Andrey Shchukarev at Umeå University for help with the XPS measurements. The authors also wish to express their gratitude to the reviewers for helpful comments that have improved the quality of the manuscript.

Competing interests statement

The authors declare no competing financial interests.

Supplementary material

Resolution of Au evaporation

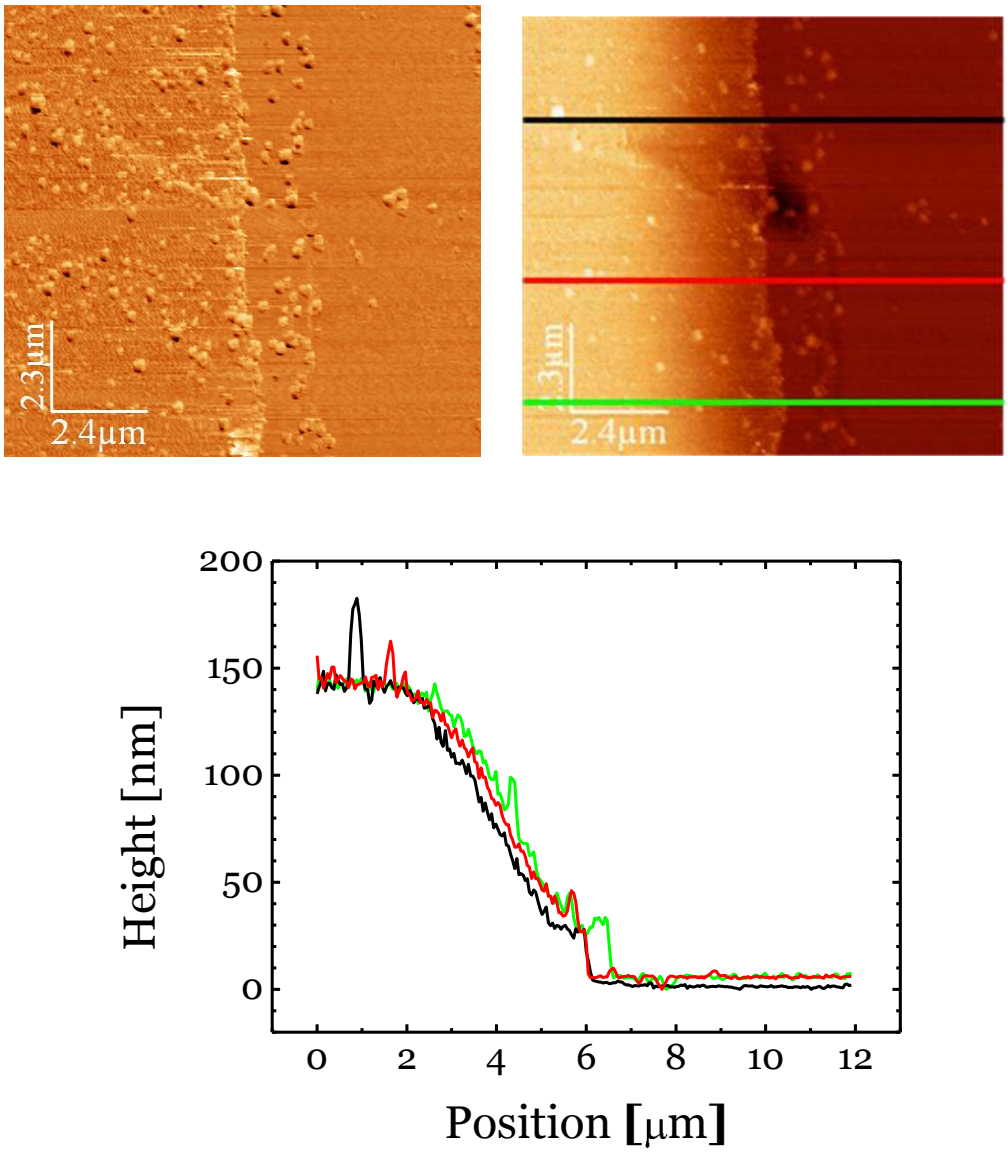

Figure S1. *AFM phase (top left) and topography (top right) images recorded at the edge of a Au electrode deposited on a glass substrate. Topography line scans (recorded at the position indicated in color in the topography image) are presented in the bottom graph. The Au electrode was deposited through the same shadow mask that was used for the fabrication of LEC devices.*

In order to assure that the position of the potential drop in the channel is not affected by a thin film of Au extending into the inter-electrode gap, we performed

tapping mode AFM on devices without an active layer. The electrodes were prepared by the same shadow masking technique as used to fabricate the devices with an active layer. Since the glass substrates are extremely flat, any Au diffusing between the electrodes, effectively reducing the gap width below the nominal value, will be visible in the AFM data. The results are shown in Fig. S1. From both the phase (left) and the topographic images (right) it is clear that the edge of the Au is sharp on the length scales that are relevant in this experiment. Topographic line sections further illustrating this are shown in the lower panel. Beyond the edge of the Au electrode at x ~ 6 micron, few scattered clusters of Au are visible in the channel, extending a few microns into the channel. Since these are evidently not connected, they do not lead to an effective reduction in the channel width.

Device current

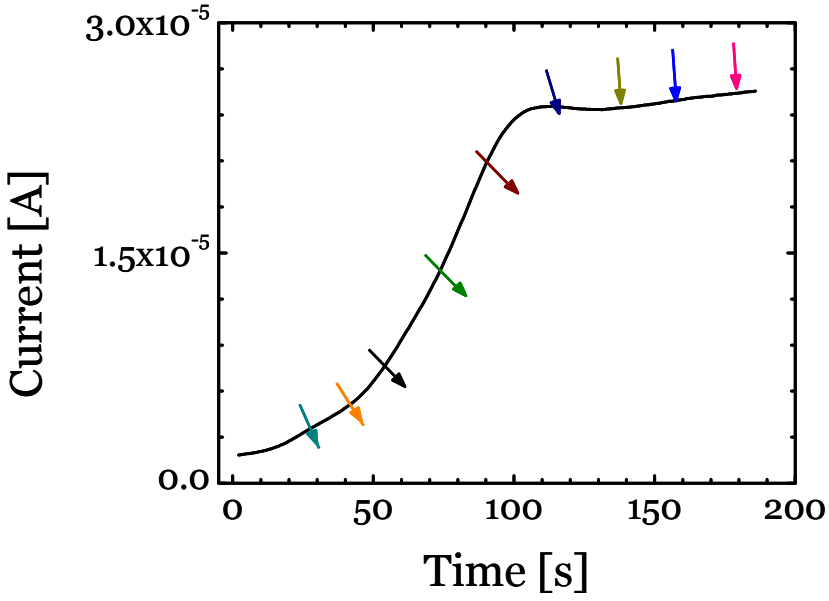

Figure S2. *Current as a function of time for a Au/{MEH-PPV+PEO+KCF_3SO_3}/Au device with a 0.12 mm inter-electrode gap during operation at V = 5V.*

The current vs. time data shown in Fig. S2 were recorded in parallel with the SKPM data presented in Figs. 2d-2e. The (colored) arrows in Fig. S2 indicate the times at which the (correspondingly colored) SKPM line scans in Fig. 2d were recorded. The observed increase in current up to t = 110 s is indicative of increasing doping within the active material of the LEC device, and is accompanied by a temporal evolution in the SKPM profiles in Fig. 2d.

Evidence for ions on top of Au electrodes

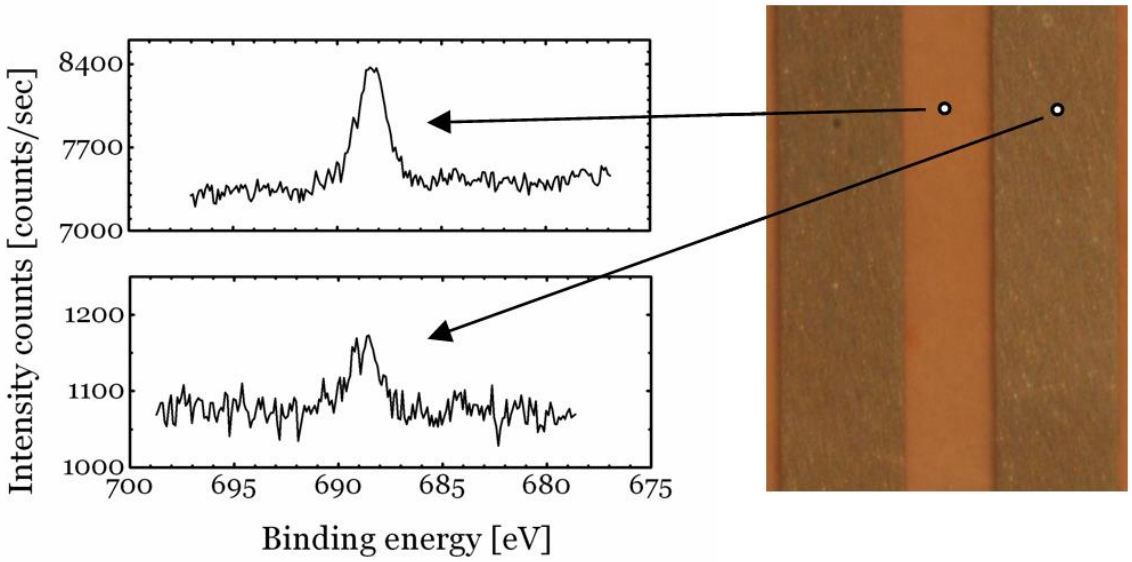

Figure S3. *XPS data (left) recorded at the marked locations in a Au/{MEH-PPV+PEO+KCF_3SO_3}/Au device with a 1 mm inter-electrode gap (photograph to the right), following long-term operation at V = 5 V. The upper graph shows data collected between the Au electrodes. The lower graph shows data collected on top of the Au electrode to the right. The spot-size of the incident X-ray beam is approximately 0.1 mm in diameter, as indicated in the photograph to the right.*

The XPS data presented in the left part of Fig. S3 were recorded following long-term operation of an LEC device at V = 5 V. The upper spectrum was recorded on the active material in the middle of the interelectrode gap (see marked location in the photograph to the right), while the bottom spectrum was recorded on top of the (previously) positively biased Au electrode at a location ~0.5 mm away from the electrode interface. The incident X-ray beam diameter of ~0.1 mm ensured that no signal from the active material in the interelectrode gap was included in the latter measurement.

The F1s core electron has a characteristic binding energy of ~688 eV, and we find fluorine present in both the active material in the inter-electrode gap and on top of the Au electrode. Since the only source of F in our experiment is the $CF_3SO_3^-$ ion, we draw the conclusion that $CF_3SO_3^-$ ions exist in the active material (as expected) and on top of the positive electrode following the operation of our LEC devices. Thus, we postulate that the lack of a potential drop at the electrode interfaces in Figs. 2 and 3 is the result of screening by ions positioned on top of the electrodes.

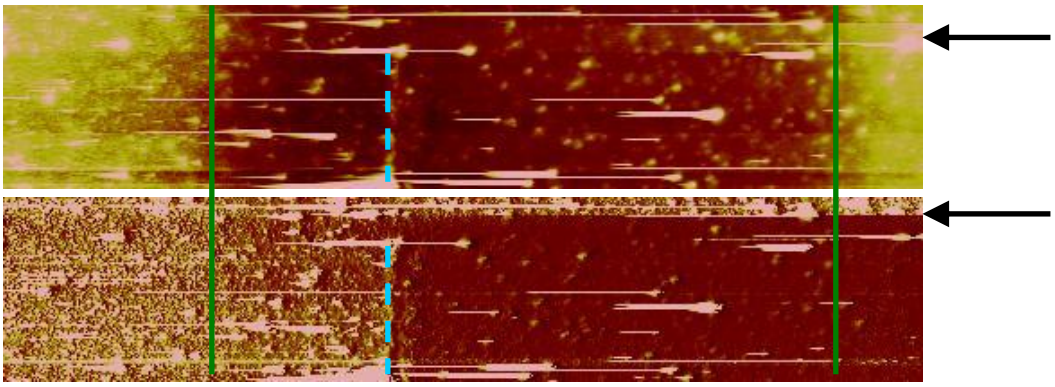

Figure S4. *Topography (top) and phase (bottom) images recorded during SKPM probing of a planar LEC device. Scan direction is from top to bottom. The green solid lines indicate the edge of the Au electrodes, and the blue dashed lines indicate the position of the p-n junction after switching on a V = +5 V bias at the position indicated by the black arrows. The positive electrode is positioned to the right.*

Before biasing the LEC device, the phase signal is relatively constant over the entire device (see the scan lines above the arrow in the bottom panel of Fig. S4). Given the difference in visco-elastic properties between the organic active material and the Au electrodes, this is quite unexpected. We interpret this as an indication that the electrodes are actually covered by a thin organic layer, despite the fact that they were deposited after spin coating. Once the device is biased, *i.e.*, below the arrows in Fig. S4, a remarkable phase signal difference between the n- and p-doped sides develops. Apparently, the p-type doping results in a change in visco-elastic properties of the organic material. It is important to point out that the (change in) phase signal extends over the positively biased electrode on the right. This confirms the notion that the electrodes are covered by a thin layer of ion-containing active material. This layer will prevent the observation of the potential drop at the electrodes by SKPM.

Many of the sharper topographic features in Fig. S4 show 'tails' in the scan direction. These are not the result of poor feedback settings; if they were, *all* topographic bumps would be smeared in a similar fashion. This is clearly not the case. The actual reason for the tails behind some sharp topographic maxima is adhesion of the tip to the active layer. This turned out to be an inherent property of the material system used, which could be reduced but not removed by optimizing the amplitude and feedback settings. The assignment of the tails to sticking rather then to suboptimal feedback settings is corroborated by the fact that several tails have a width of only one or a few scan lines whereas the corresponding topographic feature is much wider. Topographic features without tails, *i.e.,* where no sticking occurred, appear sharp and undistorted, indicating proper feedback operation.

Under these circumstances one evidently has to beware of distortions due to contamination of the tip during the experiments. However, the images show no sign of either resolution loss or sudden (or gradual) changes in the potential offset. Hence, we conclude that the tip apex remained basically unchanged during the experiments shown.

Deconvolution of SKPM cantilever / device electrode interaction

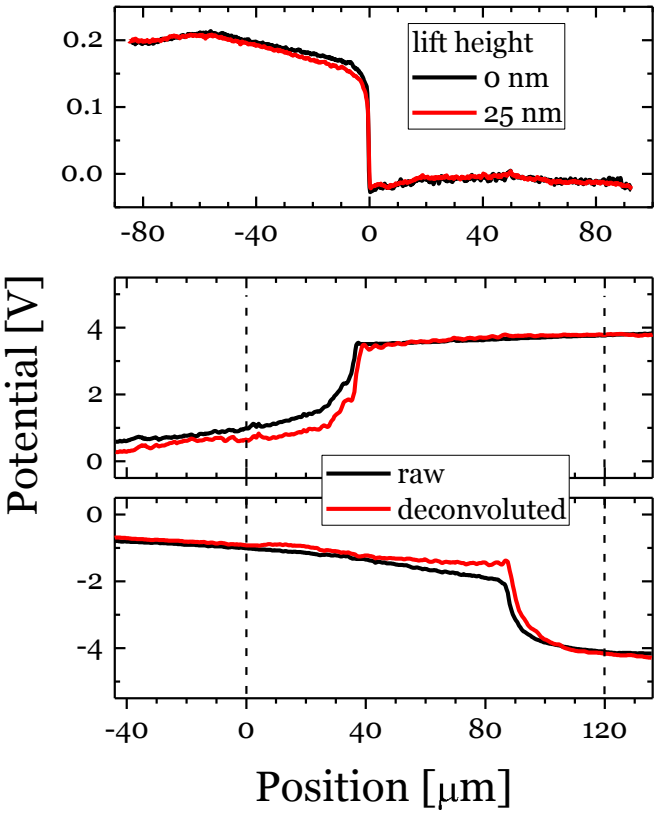

Figure S5. *Step edge response of the SKPM apparatus (top) and deconvoluted steady-state surface potentials at +5 V (middle) and -5 V (bottom). The black lines in the lower two panels represent the raw SKPM potentials, as also shown in Fig. 3 of the main text. Note that the position of the p-n junction is not affected by the non-ideal instrument response. The vertical dashed lines indicate the position of each electrode edge.*

The potential curves in Figs. 2 and 3 may not exactly follow the potential as it exists on the surface of the device. This is a common effect in SKPM, which was recently addressed in some detail. [1] Due to the electrostatic coupling between the entire device and the entire probe, consisting of cantilever, tip and apex, the true surface potential becomes convoluted with the non-ideal instrument response. In case of a

cantilever orientation perpendicular to the channel, as employed here, this can also lead to an artificial asymmetry in the measured SKPM signal. It is, however, possible to correct for the instrument response using (de)convolution in Fourier space, provided the geometry- and tip-specific transfer function *h* is known. [2] Following Ref. [2], we determined *h* on a lithographically defined step edge of 3 nm of Ti on Au, see Fig. S5. Note the asymmetric distortion due to the perpendicular tip-to-sample orientation and the enhanced broadening at the higher of the two lift heights.

For a step edge response y_{step} one has $F(h) = F(y'_{step})$, where *F*() denotes the Fourier transform and *y*' the spatial derivative of *y*. Then, the true surface potential *x* can be recovered as $x = F^{-1}\ F(y)/F(h)$. The most important conclusion of Fig. S5 is that the position of the p-n junction is not at all different after deconvolution, *i.e.,* its position is unaffected by the non-ideal instrument response. As anticipated, the field in the junction area is significantly increased after the deconvolution procedure. We also note that a finite slope in the n- and p-doped regions remains, which we attribute to the finite, but high conductivity of these regions. The higher slope in the n-doped regions indicates a lower conductivity than in the p-doped region. It is important to stress that the presence of the remaining slope is not the effect of incomplete recovery by the deconvolution procedure. This can be concluded from the fact that in absence of an electronic device current a slope of nearly zero is measured, as can be seen in Fig. 3c of the main text.

[1] D.S.H. Charrier, M. Kemerink, B.E. Smalbrugge, T. de Vries, R.A.J. Janssen, ACS Nano 2 (2008) 622.

[2] D.S.H. Charrier, T. de Vries, S.G.J. Mathijssen, E.-J. Geluk, E.C.P. Smits, M. Kemerink, R.A.J. Janssen, Org. El., in press.